energies

MDPI

Article

Virtual Vector-Based Direct Power Control of a Three-Phase Coupled Inductor-Based Bipolar-Output Active Rectifier for More Electric Aircraft

Yajun Zhao *, Wenxin Huang and Feifei Bu

College of Automation Engineering, Nanjing University of Aeronautics and Astronautics, Nanjing 210016, China
* Correspondence: zhaoyajun@nuaa.edu.cn

Abstract: Direct power control (DPC) has gained increasing attention in recent years as a simple and efficient control strategy for pulse width modulation (PWM) rectifiers. In this paper, the idea of DPC is introduced into the three-phase coupled inductor-based bipolar-output active rectifier (TCIBAR) for the first time, and a virtual vector-based direct power control (VVB-DPC) strategy is proposed for TCIBAR to realize the bipolar DC power supply for more electric aircraft (MEA). First, the mathematical model of the TCIBAR is deduced, and the basic principle of the classic DPC strategy is reviewed. On this basis, the limitations of the classic DPC strategy in TCIBAR control are analyzed. Second, a set of virtual vectors are derived to establish a novel virtual-vector switching table. Based on the virtual-vector switching table, the hysteresis power control of TCIBAR can be realized without affecting the DC-side neutral-point potential of TCIBAR. Finally, a neutral-point potential control method based on DPC architecture is studied and integrated into the VVB-DPC strategy to maintain the bipolar DC voltage balance of TCIBAR under unbalanced load conditions. The VVB-DPC strategy is experimentally studied on a TCIBAR prototype, and the experimental results verify the feasibility and effectiveness of the proposed strategy.

Keywords: direct power control; bipolar-output active rectifier; virtual vector; neutral-point potential control

Citation: Zhao, Y.; Huang, W.; Bu, F. Virtual Vector-Based Direct Power Control of a Three-Phase Coupled Inductor-Based Bipolar-Output Active Rectifier for More Electric Aircraft. *Energies* **2023**, *16*, 3038. https://doi.org/10.3390/en16073038

Academic Editor: Elhoussin Elbouchikhi

Received: 2 March 2023
Revised: 20 March 2023
Accepted: 24 March 2023
Published: 27 March 2023

1. Introduction

In recent years, more electric aircraft (MEA) have become the research trend of modern aircraft due to their higher energy efficiency, reduced maintenance costs, and lower carbon dioxide emissions [1–3]. Meanwhile, with the development of aircraft electrification, new electrical loads on aircraft will put forward higher requirements on power capacity, power quality, and power supply reliability of the electric power system (EPS) in MEA [4,5]. In order to meet the new requirements, many studies have been carried out on the architecture of the EPS in MEA [6–9], among which the ±270 V high voltage direct current (HVDC) power system is considered as a promising scheme and has attracted the interest of several research groups [10–12]. Compared to the traditional 115 V AC power system on aircraft, the ±270 V HVDC power system has the advantages of lower total weight, larger power capacity, higher reliability, and easier parallel operation of multiple sources [13,14].

In the ±270 V HVDC power system of MEA, the AC generator power is converted and transmitted to the common HVDC bus via bipolar-output rectifiers, and then the onboard electrical loads are powered by the HVDC bus directly or through power converters [7]. As can be seen, the bipolar-output rectifiers play an important role and are the key to establishing the bipolar HVDC power system for MEA. Meanwhile, in order to improve the adaptability of the EPS to unbalanced load conditions, the bipolar-output rectifier should be able to regulate the bipolar DC voltages actively and maintain the voltage balance between the bipolar DC ports. A general topology of bipolar-output active rectifier is constructed by two pulse width modulation (PWM) rectifiers connected in series at the DC port, but it

requires a transformer with two secondary windings to withstand the DC offset voltage caused by the series connection [15], which results in a significant increase in the weight of the rectifier. To solve this problem, an alternative approach is to add a voltage balancer to the output of a PWM rectifier. This topology requires only one PWM rectifier and can generate the bipolar DC outputs through the voltage balancer [16]. However, the voltage balancer cannot increase the power rating of the converter, and it still needs extra power switches and auxiliary systems, which will lead to the increase in power loss, cost, and complexity of the converter [17].

In order to establish the bipolar DC power system with a simplified converter topology, a three-phase coupled inductor-based bipolar-output active rectifier (TCIBAR) has been proposed and researched in [18,19]. The topology of TCIBAR can be simply constructed by adding a three-phase coupled inductor (TCI) to the conventional PWM rectifier, and the TCI is connected between the neutral points of the three-phase bridges and the neutral point of the DC-side split capacitors [18]. Compared to the conventional PWM rectifier, the TCI can provide a new current-injection path to the neutral point of the split capacitors. Thus, by controlling the zero-sequence current in TCI, the current injected into the DC-side neutral point can be regulated. On this basis, the TCIBAR can actively adjust the DC-side neutral-point potential and realize the voltage balance control of the bipolar DC ports under different load conditions [19]. In addition, compared with the two conventional bipolar-output active rectifiers mentioned above, TCIBAR has the advantages of fewer power switches, less complexity, and higher reliability [18]. However, it needs to achieve the same target function with a simpler topology, which will inevitably put forward higher requirements for its control strategy. Therefore, an appropriate and effective control strategy is the key to the reliable operation of the TCIBAR.

For the PWM rectifier with unipolar DC output, the control strategies can generally be categorized into voltage-oriented control (VOC) and direct power control (DPC) [20,21]. In VOC, the three-phase AC currents are transformed into d-axis and q-axis DC components in the synchronous rotating reference frame, and PI controllers are usually employed to regulate the dq-axes currents and calculate the voltage reference [22]. Then, the obtained voltage reference can be modulated by space vector modulation (SVM). VOC shows good steady-state performance, but its dynamic behavior is highly dependent on the performance of the inner current loop and phase-locked loop [22,23]. In contrast to VOC, DPC directly takes the instantaneous active and reactive power of the converter as the control variables, and it selects the appropriate voltage vector to control the instantaneous power based on the pre-established switching table and the grid voltage angular position [24–26]. As can be seen, DPC eliminates the inner current loop, phase-locked loop, and PWM generation module [27]. Meanwhile, it can achieve fast dynamic response of the rectifier with simple control architecture [27–29].

Obviously, applying DPC to the TCIBAR can share the advantages of DPC strategy and TCIBAR topology, and it can build a promising and competitive solution for the bipolar-output rectification in MEA. However, the research on DPC for bipolar-output active rectifiers is rare, and there is no DPC strategy applicable to the TCIBAR at present. Therefore, it is necessary and meaningful to explore a feasible DPC strategy for the TCIBAR.

In order to introduce the idea of DPC into the TCIBAR, the mathematical model of the TCIBAR is deduced and the basic principle of the classic DPC strategy is reviewed. However, the classic DPC strategy does not consider the influence of the zero-sequence voltage (ZSV) components in voltage vectors on the converter, which will lead to an uncontrollable zero-sequence current in TCI. Moreover, the classic DPC strategy does not involve the neutral-point potential control of the bipolar-output active rectifier, so it cannot maintain the voltage balance between bipolar DC ports, especially in the case of unbalanced port loads. Therefore, the reliable operation of TCIBAR cannot be guaranteed if the classic DPC strategy is directly applied to the TCIBAR. To overcome these shortcomings, a virtual vector-based direct power control (VVB-DPC) strategy is proposed for the TCIBAR in this

paper, and the control architecture based on DPC is constructed for the TCIBAR for the first time.

The main innovations of the proposed VVB-DPC strategy are summarized as follows. First, a set of virtual vectors, which contain the same ZSV component, are derived based on the vector synthesis of adjacent non-zero voltage vectors. Second, by analyzing the effect of the virtual vectors on the power variation of TCIBAR, a virtual-vector switching table is established for the TCIBAR. Based on the virtual-vector switching table, the VVB-DPC strategy can realize the hysteresis power control of TCIBAR without causing the runaway of the zero-sequence current in TCI. Finally, in order to maintain the voltage balance between the bipolar DC ports of TCIBAR, a neutral-point potential control method based on DPC architecture is designed and integrated into the proposed VVB-DPC strategy. By inserting an appropriate zero vector with a certain duration in one control period, the proposed neutral-point potential control method can accurately generate the required ZSV without voltage modulation module and realize the regulation of the DC-side neutral-point potential of TCIBAR.

The rest of this paper is organized as follows. Section 2 deduces the mathematical model of the TCIBAR, and the limitations of the classic DPC strategy in TCIBAR control are analyzed in Section 3. In Section 4, the proposed VVB-DPC strategy for TCIBAR is introduced in detail. Section 5 presents the simulation results of the proposed VVB-DPC strategy. Experimental research is carried out to verify the feasibility and effectiveness of the proposed VVB-DPC strategy in Section 6. Finally, the conclusions are drawn in Section 7.

2. Mathematical Model of TCIBAR

The main circuit topology of TCIBAR is depicted in Figure 1. As can be seen, the TCIBAR consists of a two-level voltage source converter (VSC) and a symmetrical TCI. Meanwhile, it contains two branches in the topology, which are defined as AC-source branch and TCI branch in this paper. In Figure 1, S_A~S_C and S'_A~S'_C are the upper and lower switches of the VSC, respectively, and R_s and R are the winding resistance of the filter inductor and the TCI. In addition, a three-phase AC source is used as the power supply instead of a generator.

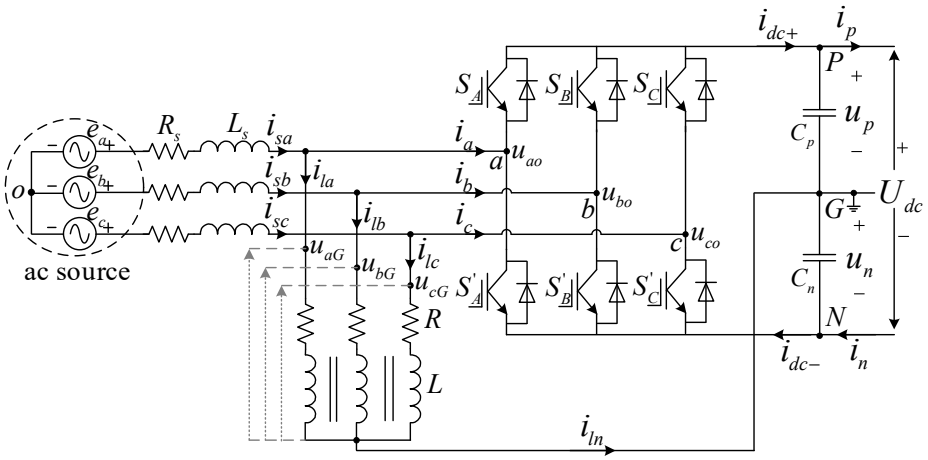

Figure 1. Main circuit topology of TCIBAR.

In order to realize the effective and comprehensive control of TCIBAR, both the AC-source branch and the TCI branch need to be modeled and analyzed. Meanwhile, since the TCI provides a zero-sequence current path for the converter, the zero-sequence components in the circuit should be taken into account when establishing the mathematical model.

According to the reference directions of the voltages and currents in Figure 1, the voltage equations of the AC-source branch can be written as follows:

$$\begin{bmatrix} e_a \\ e_b \\ e_c \end{bmatrix} = L_s \frac{d}{dt} \begin{bmatrix} i_{sa} \\ i_{sb} \\ i_{sc} \end{bmatrix} + R_s \begin{bmatrix} i_{sa} \\ i_{sb} \\ i_{sc} \end{bmatrix} + \begin{bmatrix} u_{ao} \\ u_{bo} \\ u_{co} \end{bmatrix} \tag{1}$$

where e_a, e_b, and e_c are the three-phase voltages of the AC source, u_{ao}, u_{bo}, and u_{co} are the three-phase output voltages of the VSC, and i_{sa}, i_{sb}, and i_{sc} are the three-phase input currents of the TCIBAR.

By applying the Park transformation, the voltage equations in Equation (1) can be transformed into the *dq0* coordinate system and expressed as

$$\begin{bmatrix} e_d \\ e_q \\ e_0 \end{bmatrix} = L_s \frac{d}{dt} \begin{bmatrix} i_{sd} \\ i_{sq} \\ i_{s0} \end{bmatrix} + \begin{bmatrix} 0 & -\omega L_s & 0 \\ \omega L_s & 0 & 0 \\ 0 & 0 & 0 \end{bmatrix} \begin{bmatrix} i_{sd} \\ i_{sq} \\ i_{s0} \end{bmatrix} + R_s \begin{bmatrix} i_{sd} \\ i_{sq} \\ i_{s0} \end{bmatrix} + \begin{bmatrix} u_d \\ u_q \\ u_0 \end{bmatrix} \tag{2}$$

where ω is the angular frequency of the AC source and the zero-sequence equation can be removed since $i_{s0} = 0$.

Meanwhile, based on the instantaneous power theory, the instantaneous active and reactive power of the TCIBAR can be expressed as Equation (3) in the *dq* coordinate system,

$$\begin{cases} p = e_d i_{sd} + e_q i_{sq} \\ q = e_q i_{sd} - e_d i_{sq} \end{cases} \tag{3}$$

where p and q are the active and reactive power of the TCIBAR, respectively.

In order to simplify the model and facilitate the subsequent analysis, the *dq* coordinate system is oriented by the AC-source voltage vector, and thus the q-axis component of the AC-source voltage is equal to zero, that is, $e_q = 0$. Then, by differentiating both sides of Equation (3), the active and reactive power variation rate of the TCIBAR can be written as

$$\begin{cases} \frac{dp}{dt} = i_{sd} \frac{de_d}{dt} + e_d \frac{di_{sd}}{dt} \\ \frac{dq}{dt} = -i_{sq} \frac{de_d}{dt} - e_d \frac{di_{sq}}{dt} \end{cases} \tag{4}$$

Regarding the AC source as an ideal voltage source, the d-axis voltage e_d is a constant value, that is, $de_d/dt = 0$. Substituting Equation (2) into Equation (4), the power model of the TCIBAR in the *dq* coordinate system can be deduced as

$$\begin{cases} L_s \frac{dp}{dt} = -R_s p - \omega L_s q - e_d u_d + e_d^2 \\ L_s \frac{dq}{dt} = -R_s q + \omega L_s p + e_d u_q \end{cases} \tag{5}$$

Next, in order to realize the voltage balance control of the bipolar DC ports in TCIBAR, the voltage equations of the TCI branch are derived as

$$\begin{bmatrix} u_{aG} \\ u_{bG} \\ u_{cG} \end{bmatrix} = L_{TCI} \frac{d}{dt} \begin{bmatrix} i_{la} \\ i_{lb} \\ i_{lc} \end{bmatrix} + R_{TCI} \begin{bmatrix} i_{la} \\ i_{lb} \\ i_{lc} \end{bmatrix} \tag{6}$$

where u_{aG}, u_{bG}, and u_{cG} are the three-phase voltages across the TCI, and L_{TCI} and R_{TCI} are the inductance matrix and winding resistance matrix of the TCI, respectively.

As analyzed in [19], the zero-sequence current in TCI can be controlled to maintain the voltage balance between the bipolar DC ports of TCIBAR. Meanwhile, a large zero-sequence current will flow through the TCI when the loads at the bipolar DC ports are seriously unbalanced. In order to reduce the probability of core saturation caused by the zero-sequence current, a balanced three-phase magnetic core, which cannot carry zero-

sequence DC flux [18], is applied to the TCI, and the corresponding inductance matrix and winding resistance matrix of the TCI are shown in Equation (7):

$$\begin{cases} L_{TCI} = \begin{bmatrix} L & -M & -M \\ -M & L & -M \\ -M & -M & L \end{bmatrix} \\ R_{TCI} = \begin{bmatrix} R & 0 & 0 \\ 0 & R & 0 \\ 0 & 0 & R \end{bmatrix} \end{cases} \tag{7}$$

where L and M are the self-inductance and mutual inductance of the TCI.

By substituting Equation (7) into Equation (6) and applying the Park transformation, the voltage equations of the TCI branch in $dq0$ coordinate system can be derived as

$$\begin{bmatrix} u_{ld} \\ u_{lq} \\ u_{l0} \end{bmatrix} = \begin{bmatrix} L+M & 0 & 0 \\ 0 & L+M & 0 \\ 0 & 0 & L-2M \end{bmatrix} \frac{d}{dt} \begin{bmatrix} i_{ld} \\ i_{lq} \\ i_{l0} \end{bmatrix} + \begin{bmatrix} 0 & -\omega(L+M) & 0 \\ \omega(L+M) & 0 & 0 \\ 0 & 0 & 0 \end{bmatrix} \begin{bmatrix} i_{ld} \\ i_{lq} \\ i_{l0} \end{bmatrix} + R \begin{bmatrix} i_{ld} \\ i_{lq} \\ i_{l0} \end{bmatrix} \tag{8}$$

It can be seen from Equation (8) that the TCI with a balanced three-phase magnetic core has large dq-axes inductances and a small zero-sequence inductance. The large dq-axes inductances bring the advantages of reduced dq-axes currents and lower power loss, and the small zero-sequence inductance is conductive to the fast response of the zero-sequence current in TCI. Besides, according to the zero-sequence equation in Equation (8), it can be concluded that the zero-sequence current in TCI directly depends on the ZSV across the TCI. Therefore, the accurate control of the ZSV is the key to the effective regulation of the DC-side neutral-point potential of TCIBAR.

3. Limitations of Classic DPC in TCIBAR Control

In order to introduce the control architecture of DPC into the TCIBAR, the basic principle of the classic DPC strategy is reviewed first. The classic DPC strategy has been widely used in the control of three-phase PWM rectifiers, and its control diagram is represented in Figure 2.

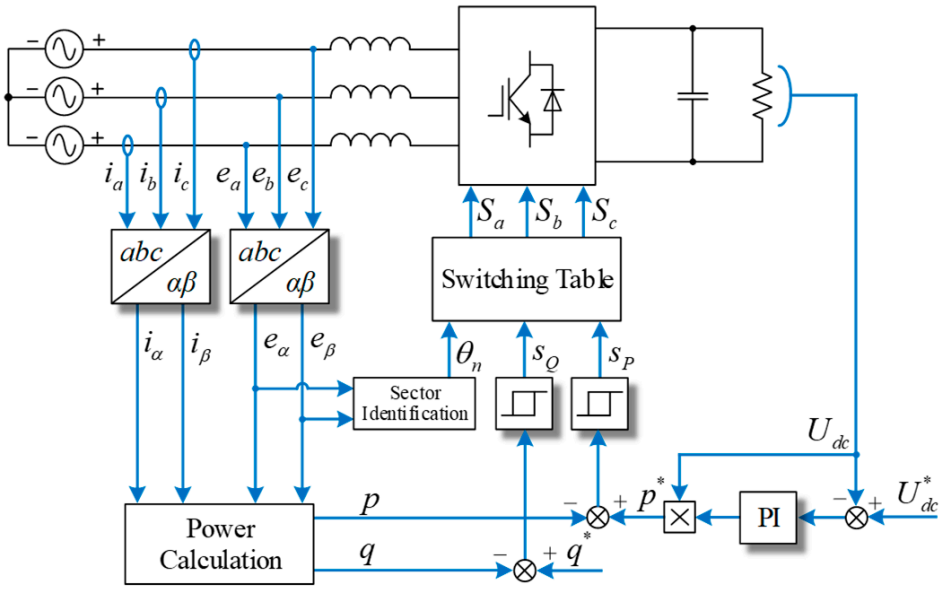

Figure 2. Control diagram of the classic DPC strategy. The superscript * represents the reference value of the variable.

In the classic DPC strategy, the hysteresis power control is employed to realize the regulation of the DC-side bus voltage and the AC-side power factor of three-phase PWM rectifiers [28]. It can be seen from Figure 2 that the classic DPC strategy consists of five main parts, which are switching table, sector identification, power calculation, hysteresis power control, and DC bus voltage control. First, the instantaneous active and reactive power of the rectifier can be calculated based on the instantaneous power theory. In the meantime, the reference value of active power p^* is obtained by the closed-loop control of DC bus voltage, and the reactive power reference q^* is usually set as zero to achieve the unit power factor of the converter. According to the instantaneous power errors, the outputs of the power hysteresis comparators are determined. Then, in order to identify the angular position of the AC-source voltage vector, the vector space is evenly divided into twelve sectors, as shown in Figure 3, and the sector boundaries are defined as

$$\frac{(n-2)\pi}{6} \leq \theta_n < \frac{(n-1)\pi}{6},\ n = 1, 2, 3, \cdots, 12 \tag{9}$$

where θ_n is the sector number.

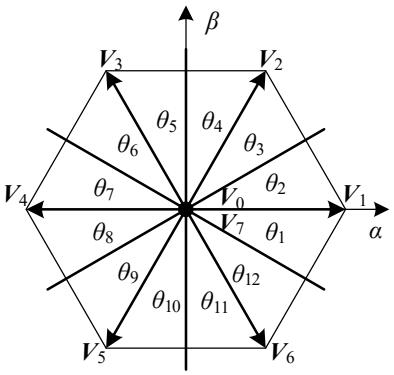

Figure 3. Sector division in the classic DPC strategy.

By calculating the phase angle of the AC-source voltage vector, the corresponding sector number can be determined. Finally, according to the outputs of the hysteresis comparators and the sector number, the desired voltage vector can be selected from the pre-defined switching table, which is established based on the effect of the basic voltage vectors ($\boldsymbol{V}_0$~$\boldsymbol{V}_7$) on the active and reactive power of the rectifier. The switching table of the classic DPC strategy is shown in Table 1, where s_P and s_Q are the outputs of the active and reactive hysteresis comparators, respectively. In [30–32], several new switching tables have been proposed for PWM rectifiers based on different optimization objectives, and it can be seen that the switching table affects the performance of the DPC strategy directly and is the key to the DPC strategy.

Table 1. Switching table of Classic DPC strategy.

s_P	s_Q	θ_1	θ_2	θ_3	θ_4	θ_5	θ_6	θ_7	θ_8	θ_9	θ_{10}	θ_{11}	θ_{12}
0	0	$\boldsymbol{V}_6$	$\boldsymbol{V}_1$	$\boldsymbol{V}_1$	$\boldsymbol{V}_2$	$\boldsymbol{V}_2$	$\boldsymbol{V}_3$	$\boldsymbol{V}_3$	$\boldsymbol{V}_4$	$\boldsymbol{V}_4$	$\boldsymbol{V}_5$	$\boldsymbol{V}_5$	$\boldsymbol{V}_6$
0	1	$\boldsymbol{V}_1$	$\boldsymbol{V}_2$	$\boldsymbol{V}_2$	$\boldsymbol{V}_3$	$\boldsymbol{V}_3$	$\boldsymbol{V}_4$	$\boldsymbol{V}_4$	$\boldsymbol{V}_5$	$\boldsymbol{V}_5$	$\boldsymbol{V}_6$	$\boldsymbol{V}_6$	$\boldsymbol{V}_1$
1	0	$\boldsymbol{V}_6$	$\boldsymbol{V}_7$	$\boldsymbol{V}_1$	$\boldsymbol{V}_0$	$\boldsymbol{V}_2$	$\boldsymbol{V}_7$	$\boldsymbol{V}_3$	$\boldsymbol{V}_0$	$\boldsymbol{V}_4$	$\boldsymbol{V}_7$	$\boldsymbol{V}_5$	$\boldsymbol{V}_0$
1	1	$\boldsymbol{V}_7$	$\boldsymbol{V}_7$	$\boldsymbol{V}_0$	$\boldsymbol{V}_0$	$\boldsymbol{V}_7$	$\boldsymbol{V}_7$	$\boldsymbol{V}_0$	$\boldsymbol{V}_0$	$\boldsymbol{V}_7$	$\boldsymbol{V}_7$	$\boldsymbol{V}_0$	$\boldsymbol{V}_0$

However, based on the observation of the above control diagram and switching table, it can be found that the classic DPC strategy has two limitations in the control of TCIBAR. First, since there is no zero-sequence current in the general three-phase PWM rectifiers, the classic DPC strategy does not need to consider the influence of different ZSV components in the basic voltage vectors on the rectifier. If classic DPC strategy is directly applied to the

TCIBAR, it will inevitably result in an uncontrollable zero-sequence current in TCI, which will further cause the loss of control of the DC-side neutral-point potential and even lead to the oscillation and instability of the converter. Second, for the TCIBAR with bipolar DC outputs, it not only needs to ensure the stability of the total DC bus voltage, but also needs to regulate the neutral-point potential of the bipolar DC ports and maintain the voltage balance under unbalanced load conditions, which is not taken into account in the classic DPC strategy. Therefore, the classic DPC strategy is not applicable for the TCIBAR, and a VVB-DPC strategy will be proposed and detailed in the next section.

4. Proposed VVB-DPC for TCIBAR

In order to break through the limitations of the classic DPC and implement the DPC strategy in TCIBAR, the concept of virtual vector is introduced to extend the original voltage vectors, and a VVB-DPC strategy with the ability to regulate the neutral-point potential is explored for the TCIBAR in this section.

4.1. Derivation of Virtual Vector

An effective solution to the first problem mentioned above is to search for a set of new voltage vectors that contain the same ZSV component, so that the change in the selected voltage vectors will not affect the ZSV across the TCI. In order to find the new voltage vectors that meet the requirement, the ZSVs of the eight basic voltage vectors are deduced first.

By defining the switching function of the three-phase bridges in TCIBAR as Sx ($x = a, b, c$), the three-phase voltages across the TCI can be expressed as

$$\begin{cases} u_{aG} = S_a U_{dc} - \varepsilon U_{dc} \\ u_{bG} = S_b U_{dc} - \varepsilon U_{dc} \\ u_{cG} = S_c U_{dc} - \varepsilon U_{dc} \end{cases} \tag{10}$$

where $S_x = 0$ and $S_x = 1$ correspond to the on-state and off-state of the upper switch in the phase bridge x, respectively. Besides, ε ($0 < \varepsilon < 1$) is defined as the voltage coefficient of the DC-side neutral point, and εU_{dc} is the actual voltage of the negative DC port of TCIBAR.

Then, by applying the Park transformation to Equation (10), the ZSV applied to the TCI can be calculated as follows

$$u_{l0} = [\frac{1}{\sqrt{3}}(S_a + S_b + S_c) - \sqrt{3}\varepsilon]U_{dc} \tag{11}$$

Substituting the switching states of the eight basic voltage vectors into Equation (11), the corresponding ZSV component in each basic voltage vector can be obtained and shown in Table 2.

Table 2. ZSV components in basic voltage vectors.

Vectors	S_a	S_b	S_c	u_{l0}
V_0	0	0	0	$-\sqrt{3}\varepsilon U_{dc}$
V_1	1	0	0	$(1/\sqrt{3} - \sqrt{3}\varepsilon)U_{dc}$
V_2	1	1	0	$(2/\sqrt{3} - \sqrt{3}\varepsilon)U_{dc}$
V_3	0	1	0	$(1/\sqrt{3} - \sqrt{3}\varepsilon)U_{dc}$
V_4	0	1	1	$(2/\sqrt{3} - \sqrt{3}\varepsilon)U_{dc}$
V_5	0	0	1	$(1/\sqrt{3} - \sqrt{3}\varepsilon)U_{dc}$
V_6	1	0	1	$(2/\sqrt{3} - \sqrt{3}\varepsilon)U_{dc}$
V_7	1	1	1	$\sqrt{3}(1 - \varepsilon)U_{dc}$

As can be seen from Table 2, the ZSV components in different basic voltage vectors are not all the same and have four different cases: $-\sqrt{3}\varepsilon U_{dc}$ in $\boldsymbol{V}_0$, $(1/\sqrt{3}-\sqrt{3}\varepsilon)U_{dc}$ in $\boldsymbol{V}_1$, $\boldsymbol{V}_3$, $\boldsymbol{V}_5$, $(2/\sqrt{3}-\sqrt{3}\varepsilon)U_{dc}$ in $\boldsymbol{V}_2$, $\boldsymbol{V}_4$, $\boldsymbol{V}_6$ and $\sqrt{3}(1-\varepsilon)U_{dc}$ in $\boldsymbol{V}_7$. Meanwhile, it can be found that, among the six non-zero voltage vectors, any two adjacent non-zero voltage vectors always generate the ZSVs of $(1/\sqrt{3}-\sqrt{3}\varepsilon)U_{dc}$ and $(2/\sqrt{3}-\sqrt{3}\varepsilon)U_{dc}$. Based on this observation, a set of virtual vectors, which are synthesized by every two adjacent non-zero voltage vectors, are proposed to extend the original voltage vectors, and the virtual vector $\boldsymbol{V}_{mn}$ is denoted as

$$V_{mn} = \frac{t_m}{T_s}V_m + \frac{t_n}{T_s}V_n \tag{12}$$

where $\boldsymbol{V}_m$ and $\boldsymbol{V}_n$ are the adjacent non-zero voltage vectors, T_s is the control cycle, and t_m and t_n are the action time of $\boldsymbol{V}_m$ and $\boldsymbol{V}_n$ in one control cycle. Meanwhile, the sum of t_m and t_n is equal to T_s.

Defining $\boldsymbol{V}_1$, $\boldsymbol{V}_3$, and $\boldsymbol{V}_5$ as odd vectors and $\boldsymbol{V}_2$, $\boldsymbol{V}_4$, and $\boldsymbol{V}_6$ as even vectors, it can be seen that the virtual vectors are synthesized by adjacent odd and even vectors in one control cycle. At the same time, the ZSV components in the odd and even vectors are $(1/\sqrt{3}-\sqrt{3}\varepsilon)U_{dc}$ and $(2/\sqrt{3}-\sqrt{3}\varepsilon)U_{dc}$, respectively. Therefore, in order to make the ZSV component in each virtual vector equal, the odd and even vectors of each virtual vector should have the same action time ratio in one control cycle. In this paper, the action time of the even and odd vectors are set as λT_s and $(1-\lambda)T_s$, respectively, where λ ($0 \le \lambda \le 1$) is the time coefficient. On this basis, the switching functions of the virtual vectors, as well as the corresponding ZSV components, can be deduced based on the volt-second equivalent principle, as shown in Table 3.

Table 3. Switching functions and ZSV components of virtual vectors.

Vectors	S_a	S_b	S_c	u_{l0}
$\boldsymbol{V}_{12}$	1	$1-\lambda$	0	$(2-\lambda-3\varepsilon)U_{dc}/\sqrt{3}$
$\boldsymbol{V}_{23}$	$1-\lambda$	1	0	$(2-\lambda-3\varepsilon)U_{dc}/\sqrt{3}$
$\boldsymbol{V}_{34}$	0	1	$1-\lambda$	$(2-\lambda-3\varepsilon)U_{dc}/\sqrt{3}$
$\boldsymbol{V}_{45}$	0	$1-\lambda$	1	$(2-\lambda-3\varepsilon)U_{dc}/\sqrt{3}$
$\boldsymbol{V}_{56}$	$1-\lambda$	0	1	$(2-\lambda-3\varepsilon)U_{dc}/\sqrt{3}$
$\boldsymbol{V}_{61}$	1	0	$1-\lambda$	$(2-\lambda-3\varepsilon)U_{dc}/\sqrt{3}$

It can be seen, from Table 3, that six virtual vectors can be synthesized by adjacent non-zero voltage vectors, and the virtual vectors have the same ZSV component, which can be expressed as

$$u_{l0} = (2-\lambda-3\varepsilon)U_{dc}/\sqrt{3} \tag{13}$$

Besides, in order to realize the hysteresis power control of TCIBAR without affecting the DC-side neutral-point potential, the ZSV component in each virtual vector should be equal to zero, that is, $u_{l0} = 0$. Meanwhile, considering that the bipolar DC voltages of the TCIBAR should be symmetrical in the HVDC power system of MEA, the voltage coefficient $\mathcal{E}$ should be equal to 0.5 in the steady state. Substituting $u_{l0} = 0$ and $\mathcal{E} = 0.5$ into Equation (13), the time coefficient λ can be calculated as

$$\lambda = 2 - 3\mathcal{E} - \frac{\sqrt{3}u_{l0}}{U_{dc}} = 0.5 \tag{14}$$

Therefore, the time coefficient λ is selected as 0.5 in this paper, which means that the adjacent odd and even vectors will each act for half of the control cycle to synthesize the desired virtual vectors. On this basis, the six virtual vectors adopted in this paper and their switching sequences are determined, as shown in Figure 4. When the proposed six virtual vectors are used to implement the hysteresis power control of TCIBAR, the ZSV applied to

the TCI can remain unchanged, so the zero-sequence current in the TCI will not be out of control under the action of virtual vectors.

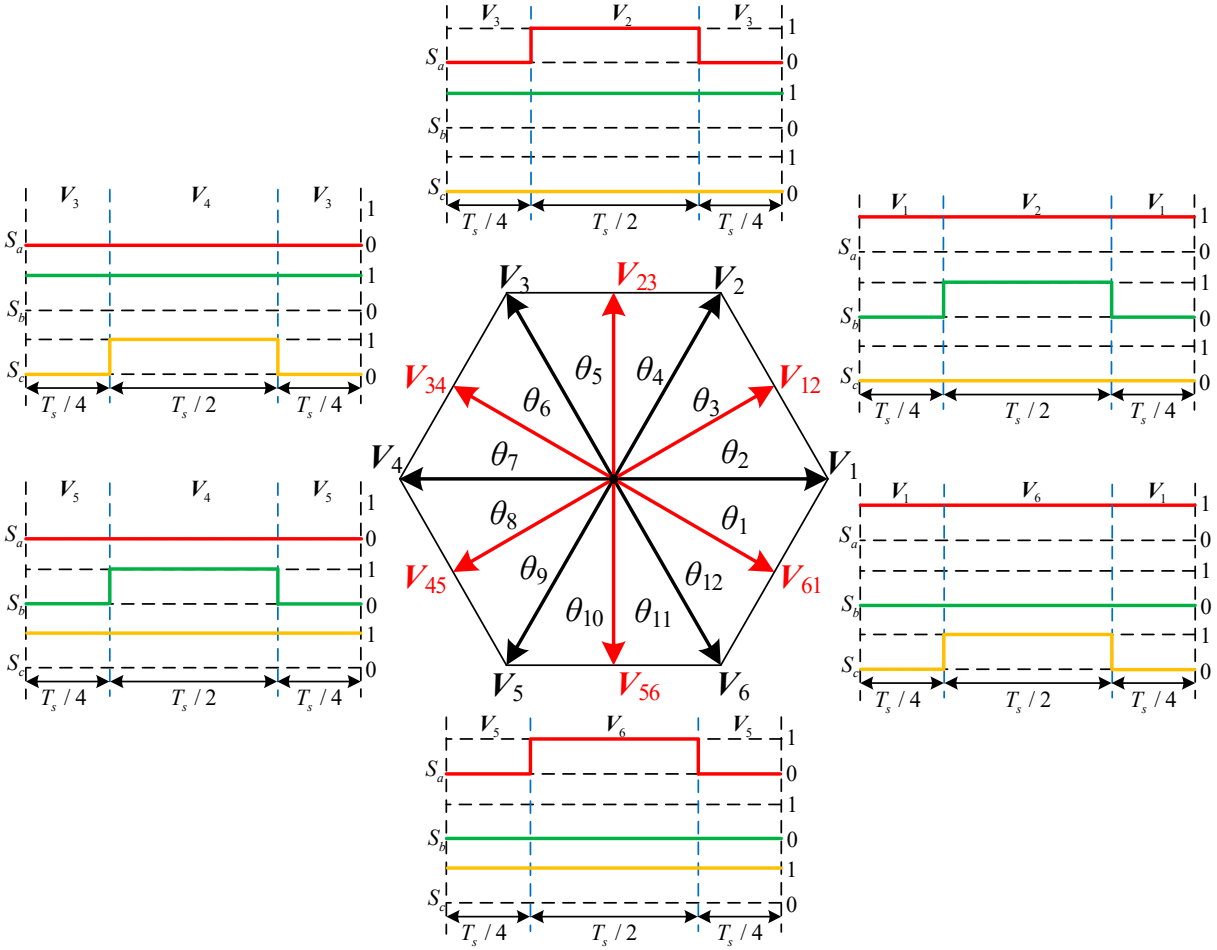

Figure 4. Proposed virtual vectors and corresponding switching sequences.

4.2. Switching Table Based on Virtual Vectors

As described in Section 3, the switching table is the key element of the DPC strategy. Therefore, in order to establish the switching table based on the virtual vectors and realize the hysteresis power control of TCIBAR, it is necessary to analyze the effect of each virtual vector on the power variation of TCIBAR.

Ignoring the winding resistance R_s, the AC-source branch of TCIBAR satisfies the vector equation in Equation (15),

$$\boldsymbol{I}_s(t) = \boldsymbol{I}_s(0) + \frac{1}{L_s}\int_0^t (\boldsymbol{E} - \boldsymbol{V}_{mn})dt \tag{15}$$

where $\boldsymbol{I}_s(0)$ and $\boldsymbol{I}_s(t)$ are the AC-source current vector at time 0 and time t, and $\boldsymbol{E}$ is the AC-source voltage vector.

Considering that the vector $\boldsymbol{E}-\boldsymbol{V}_{mn}$ remains almost unchanged in one control cycle T_s, the variation of the AC-source current vector ($\Delta\boldsymbol{I}_s$) in a control cycle can be deduced according to Equation (15), as shown in Equation (16).

$$\Delta\boldsymbol{I}_s = \frac{T_s}{L_s}(\boldsymbol{E} - \boldsymbol{V}_{mn}) \tag{16}$$

In addition, based on the power calculation formula in the dq coordinate system, the power variation in one control cycle can be calculated as

$$\begin{cases} \Delta p = |\boldsymbol{E}|\Delta I_d = |\boldsymbol{E}||\Delta \boldsymbol{I}_s|\cos\gamma \\ \Delta q = -|\boldsymbol{E}|\Delta I_q = -|\boldsymbol{E}||\Delta \boldsymbol{I}_s|\sin\gamma \end{cases} \tag{17}$$

where ΔI_d and ΔI_q are the projection components of $\Delta \boldsymbol{I}_s$ on the d-axis and q-axis, and γ is the angle between $\Delta \boldsymbol{I}_s$ and the d-axis.

By substituting Equation (16) into Equation (17), the relationship between the vector $\boldsymbol{E}-\boldsymbol{V}_{mn}$ and the power variation can be obtained as follows:

$$\begin{cases} \Delta p = \frac{T_s}{L_s}|\boldsymbol{E}||\boldsymbol{E}-\boldsymbol{V}_{mn}|\cos\gamma \\ \Delta q = -\frac{T_s}{L_s}|\boldsymbol{E}||\boldsymbol{E}-\boldsymbol{V}_{mn}|\sin\gamma \end{cases} \tag{18}$$

It can be seen from Equation (18) that the active power variation depends on the projection of $\boldsymbol{E}-\boldsymbol{V}_{mn}$ on the d-axis, while the reactive power variation is determined by the projection of $\boldsymbol{E}-\boldsymbol{V}_{mn}$ on the q-axis. Therefore, the effect of each virtual vector on the power variation of TCIBAR can be obtained according to the direction and amplitude of the projection of $\boldsymbol{E}-\boldsymbol{V}_{mn}$ on the d-axis and q-axis. Taking the AC-source voltage vector $\boldsymbol{E}$ in the sector θ_3 as an example, the effect of different voltage vectors on the power variation of TCIBAR can be analyzed, and Figure 5a shows the effect of the virtual vector $\boldsymbol{V}_{56}$. In the meantime, the vector space can be divided into four areas according to the signs of the active and reactive power variation rates, as shown in Figure 5b.

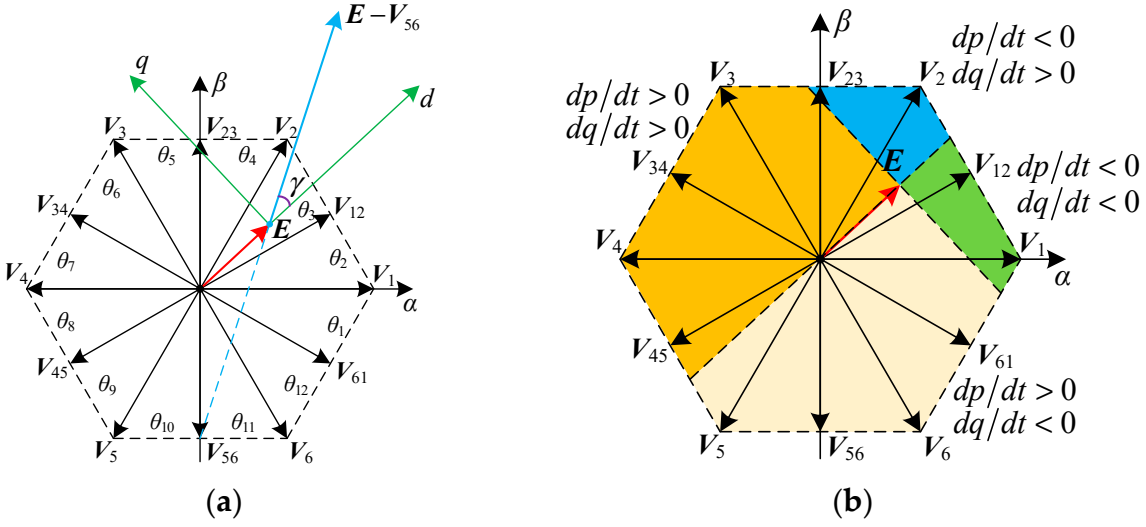

Figure 5. Effect of voltage vectors on power variation of TCIBAR when $\boldsymbol{E}$ in sector θ_3. (**a**) Effect of $\boldsymbol{V}_{56}$. (**b**) Area division based on power variation rate.

It can be seen from Figure 5b that when the AC-source voltage vector $\boldsymbol{E}$ is in the sector θ_3, the virtual vectors $\boldsymbol{V}_{34}$, $\boldsymbol{V}_{45}$, $\boldsymbol{V}_{56}$, and $\boldsymbol{V}_{61}$ will increase the active power of TCIBAR, while $\boldsymbol{V}_{12}$ and $\boldsymbol{V}_{23}$ will decrease the active power. At the same time, the reactive power of the TCIBAR will be increased by the virtual vectors $\boldsymbol{V}_{23}$, $\boldsymbol{V}_{34}$, and $\boldsymbol{V}_{45}$ and decreased by $\boldsymbol{V}_{56}$, $\boldsymbol{V}_{61}$, and $\boldsymbol{V}_{12}$. Thus, the appropriate virtual vector can be selected according to the outputs of the power hysteresis comparators. Similarly, when the AC-source voltage vector $\boldsymbol{E}$ is in other eleven sectors, the same analysis method is used to select the corresponding virtual vectors and the complete virtual-vector switching table can be established, as shown in Table 4.

Table 4. Virtual-vector switching table for VVB-DPC.

s_P	s_Q	θ_1	θ_2	θ_3	θ_4	θ_5	θ_6	θ_7	θ_8	θ_9	θ_{10}	θ_{11}	θ_{12}
0	0	V_{61}	V_{61}	V_{12}	V_{12}	V_{23}	V_{23}	V_{34}	V_{34}	V_{45}	V_{45}	V_{56}	V_{56}
0	1	V_{12}	V_{12}	V_{23}	V_{23}	V_{34}	V_{34}	V_{45}	V_{45}	V_{56}	V_{56}	V_{61}	V_{61}
1	0	V_{45}	V_{56}	V_{56}	V_{61}	V_{61}	V_{12}	V_{12}	V_{23}	V_{23}	V_{34}	V_{34}	V_{45}
1	1	V_{23}	V_{34}	V_{34}	V_{45}	V_{45}	V_{56}	V_{56}	V_{61}	V_{61}	V_{12}	V_{12}	V_{23}

Based on the virtual-vector switching table, the hysteresis power control of the TCIBAR can be realized, which results in an effective control of the DC bus voltage and AC-side power factor of the TCIBAR. Meanwhile, the DC-side neutral point potential will not be affected by the change in the selected virtual vectors.

4.3. Neutral-Point Potential Control Method Based on DPC Architecture

In order to maintain the voltage balance between the bipolar DC ports under unbalanced load conditions, a neutral-point potential control method based on DPC architecture is studied for the TCIBAR. As analyzed in Section 2, the DC-side neutral-point potential of the TCIBAR can be regulated by the closed-loop control of the zero-sequence current in TCI, which is directly determined by the ZSV across the TCI. Thus, the key to the neutral-point potential control is the generation of the reference and actual values of ZSV.

First, in order to obtain the reference ZSV, a double closed-loop control algorithm is constructed with PI controllers, and the control variables of the outer and inner loops are the voltage difference between bipolar DC ports (Δu) and the zero-sequence current in TCI (i_{l0}), respectively. Meanwhile, the PI controllers of Δu and i_{l0} can be designed by referring to the classical PI parameter design method in [33,34]. Based on this control algorithm, the reference value of ZSV can be obtained. However, since there is no voltage modulation module in the DPC architecture, the accurate generation of the actual ZSV is the critical problem in the neutral-point potential control of TCIBAR.

Substituting the switching states of six virtual vectors and two zero vectors into Equation (11), the actual ZSV components in virtual vectors and zero vectors can be derived, as shown in Table 5.

Table 5. Actual ZSV components in virtual vectors and zero vectors.

Vectors	S_a	S_b	S_c	u_{l0}
V_{12}	1	0.5	0	$\sqrt{3}(1-2\varepsilon)U_{dc}/2$
V_{23}	0.5	1	0	$\sqrt{3}(1-2\varepsilon)U_{dc}/2$
V_{34}	0	1	0.5	$\sqrt{3}(1-2\varepsilon)U_{dc}/2$
V_{45}	0	0.5	1	$\sqrt{3}(1-2\varepsilon)U_{dc}/2$
V_{56}	0.5	0	1	$\sqrt{3}(1-2\varepsilon)U_{dc}/2$
V_{61}	1	0	0.5	$\sqrt{3}(1-2\varepsilon)U_{dc}/2$
V_0	0	0	0	$-\sqrt{3}\varepsilon U_{dc}$
V_7	1	1	1	$\sqrt{3}(1-\varepsilon)U_{dc}$

It can be seen from Table 5 that the actual ZSV components in different voltage vectors are related to the neutral-point potential of the TCIBAR, which has three different cases: (1) $\sqrt{3}(1-2\varepsilon)U_{dc}/2$ in virtual vectors; (2) $\sqrt{3}(1-\varepsilon)U_{dc}$ in V_7; and (3) $-\sqrt{3}\varepsilon U_{dc}$ in V_0. Because of the constraint that $0 < \varepsilon < 1$, the ZSV components in V_0 and V_7 always have the opposite signs, and the three cases of the ZSV components satisfy the following inequality:

$$\sqrt{3}(1-\varepsilon)U_{dc} > \frac{\sqrt{3}(1-2\varepsilon)U_{dc}}{2} > -\sqrt{3}\varepsilon U_{dc} \tag{19}$$

In addition, considering that the zero vectors do not affect the reactive power of the converter and have a weak influence on the active power, the actual ZSV can be accurately generated by inserting a zero vector (V_0 or V_7) with a certain duty ratio into the selected

virtual vector within one control cycle. Meanwhile, the inserted zero vector and its action time are dependent on the reference value of the ZSV (u_{l0}^*) and can be categorized as the following two cases.

Case 1:

$$u_{l0}^* \geq \frac{\sqrt{3}(1-2\varepsilon)U_{dc}}{2} \tag{20}$$

In this case, the reference ZSV is greater than the actual ZSV component in the virtual vector. Therefore, the zero vector $\boldsymbol{V}_7$ *is inserted, and the action time can be calculated as follows:*

$$\begin{cases} u_{l0}^* T_s = \frac{\sqrt{3}(1-2\varepsilon)}{2} U_{dc} t_{mn} + \sqrt{3}(1-\varepsilon) U_{dc} t_7 \\ t_{mn} + t_7 = T_s \end{cases} \tag{21}$$

where t_{mn} *and* t_7 *are the action time of the selected virtual vector and the zero vector* $\boldsymbol{V}_7$*.*

By solving the Equation (21), the action time t_{mn} *and* t_7 *can be obtained as*

$$\begin{cases} t_7 = (\frac{2}{\sqrt{3}} \frac{u_{l0}^*}{U_{dc}} + \frac{2\varepsilon-1}{\sqrt{3}}) T_s \\ t_{mn} = \frac{2}{\sqrt{3}} (1 - \varepsilon - \frac{u_{l0}^*}{U_{dc}}) T_s \end{cases} \tag{22}$$

Case 2:

$$u_{l0}^* < \frac{\sqrt{3}(1-2\varepsilon)U_{dc}}{2} \tag{23}$$

In this case, the zero vector $\boldsymbol{V}_0$ *is inserted to synthesize the reference ZSV, and the action time can be calculated as*

$$\begin{cases} u_{l0}^* T_s = \frac{\sqrt{3}(1-2\varepsilon)}{2} U_{dc} t_{mn} - \sqrt{3}\varepsilon U_{dc} t_0 \\ t_{mn} + t_0 = T_s \end{cases} \tag{24}$$

where t_0 *is the action time of* $\boldsymbol{V}_0$*.*

Similarly, t_{mn} *and* t_0 *can be obtained as follows:*

$$\begin{cases} t_0 = [\frac{1}{\sqrt{3}} - \frac{2}{\sqrt{3}} (\frac{u_{l0}^*}{U_{dc}} + \varepsilon)] T_s \\ t_{mn} = \frac{2}{\sqrt{3}} (\frac{u_{l0}^*}{U_{dc}} + \varepsilon) T_s \end{cases} \tag{25}$$

According to the above analysis and design, the action time of the selected virtual vector and zero vector in one control cycle is obtained, and the desired ZSV can be generated accurately. On this basis, the neutral-point potential control of TCIBAR can be successfully implemented in the DPC architecture.

4.4. Overall Control Block Diagram of the Proposed VVB-DPC

Based on the above research and analysis, the overall control block diagram of the proposed VVB-DPC strategy is obtained, as shown in Figure 6.

As can be seen from Figure 6, the proposed VVB-DPC strategy mainly consists of power control and neutral-point potential control. Compared with the classic DPC strategy shown in Figure 2, the VVB-DPC strategy introduces the virtual vectors to realize the hysteresis power control of the TCIBAR and can avoid the runaway of the zero-sequence current in TCI. Besides, the neutral-point potential control of the TCIBAR can be achieved by inserting an appropriate zero vector with a certain duty ratio in one control cycle.

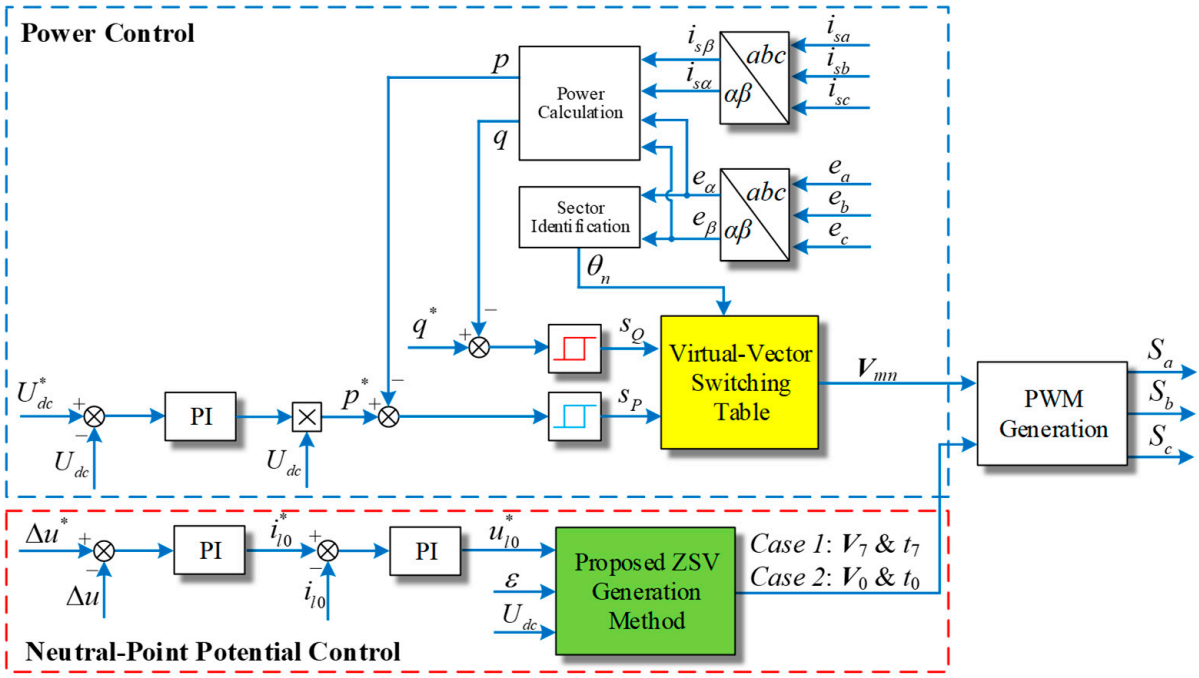

Figure 6. Control block diagram of the proposed VVB-DPC strategy. The superscript * represents the reference value of the variable.

5. Simulation Results

To verify the performance of the proposed VVB-DPC strategy, the simulation of a TCIBAR was carried out based on the software PLECS. The sampling frequency is 20 kHz, and the rated parameters of the TCIBAR are listed in Table 6, which were used in both the simulations and experiments.

Table 6. Parameters of the TCIBAR.

Parameter	Symbol	Value
Rated power	P	5 kW
Rated DC bus voltage	U_{dc}	360 V
Rated positive voltage	u_p	180 V
Rated negative voltage	u_n	180 V
RMS value of AC-source phase voltage	E_{ac}	115 V
Frequency of AC source	f_{ac}	400 Hz
Positive port capacitance	C_p	6600 μF
Negative port capacitance	C_n	6600 μF
Filter inductance	L_s	1.5 mH
Self-inductance of TCI	L	0.526 H
Mutual inductance of TCI	M	0.259 H

The simulations of the classic switching table and the proposed virtual-vector switching table have been performed, respectively, and the corresponding results are shown in Figure 7. As can be seen, the classic switching table causes an uncontrollable total zero-sequence current (i_{ln}) in the TCI and leads to a voltage imbalance between the bipolar DC ports. However, the proposed switching table does not affect the zero-sequence current in TCI and can realize the effective control of both the DC bus voltage and neutral-point potential, which verifies the feasibility of the proposed VVB-DPC strategy.

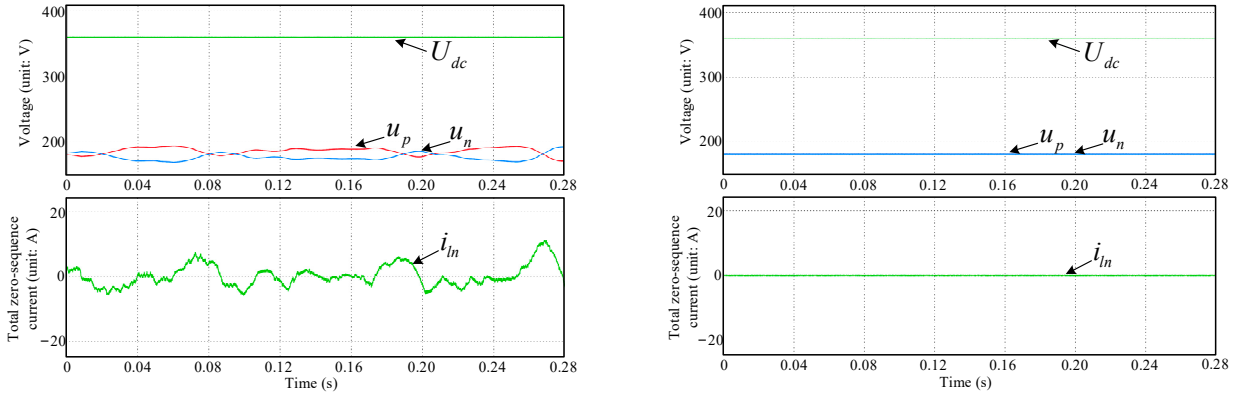

Figure 7. Simulation results of different switching tables under no-load condition. (**a**) Classic switching table. (**b**) Proposed virtual-vector switching table.

The simulation results under unbalanced load condition are shown in Figure 8, where only the negative DC port of TCIBAR is connected with a 13.3 Ω resistor. To better demonstrate the effect of the proposed neutral-point potential control method, the simulation results with and without the neutral-point potential control are presented in Figure 8a,b for comparison. It can be seen from Figure 8 that the proposed neutral-point potential control method can effectively eliminate the voltage imbalance between the bipolar DC ports under unbalanced load conditions.

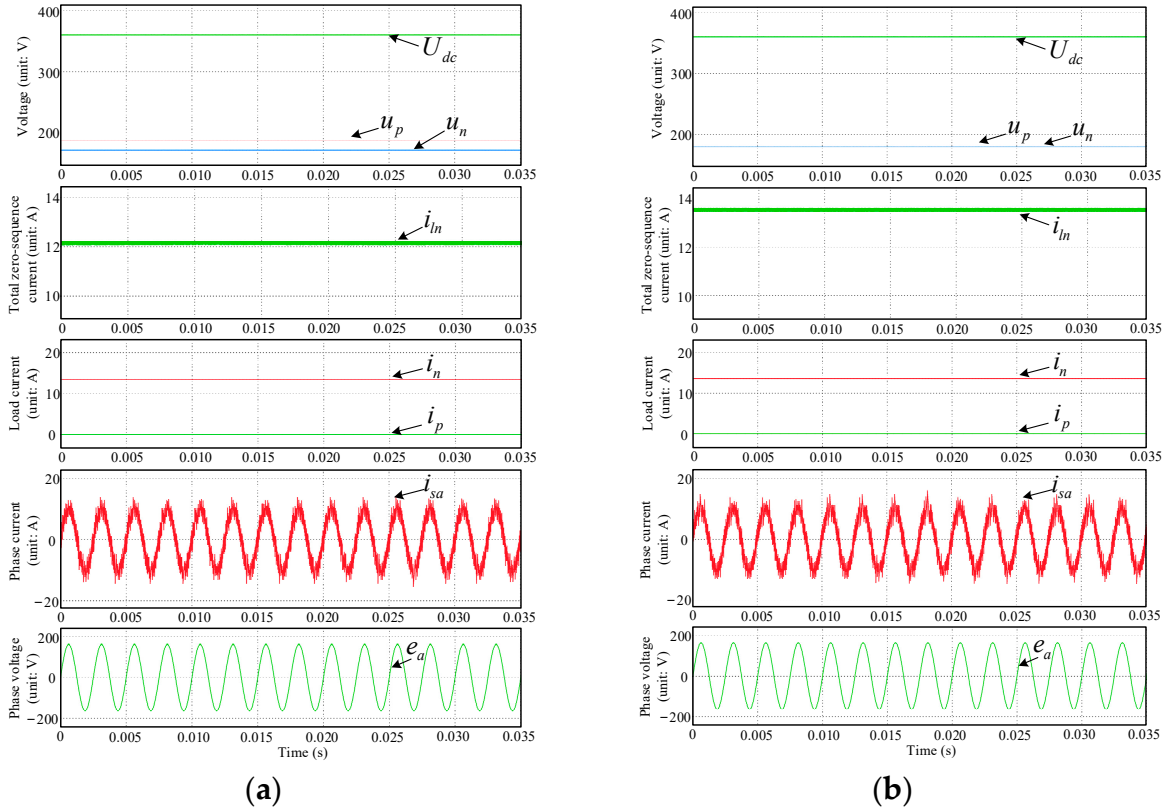

Figure 8. Simulation results under unbalanced load conditions. (**a**) Without proposed neutral-point potential control method. (**b**) With proposed neutral-point potential control method.

Figure 9 further presents the dynamic simulation results of the proposed VVB-DPC strategy under balanced and unbalanced load conditions, where the unbalanced load condition is the same as above, and the balanced load condition is constructed by connecting 13.3 Ω resistors to both the positive and negative DC ports. As can be seen, the proposed VVB-DPC strategy can not only respond immediately to restore the DC bus voltage to the rated value, but also quickly rebalance the DC voltages between the bipolar DC ports after the unbalanced load is switched on.

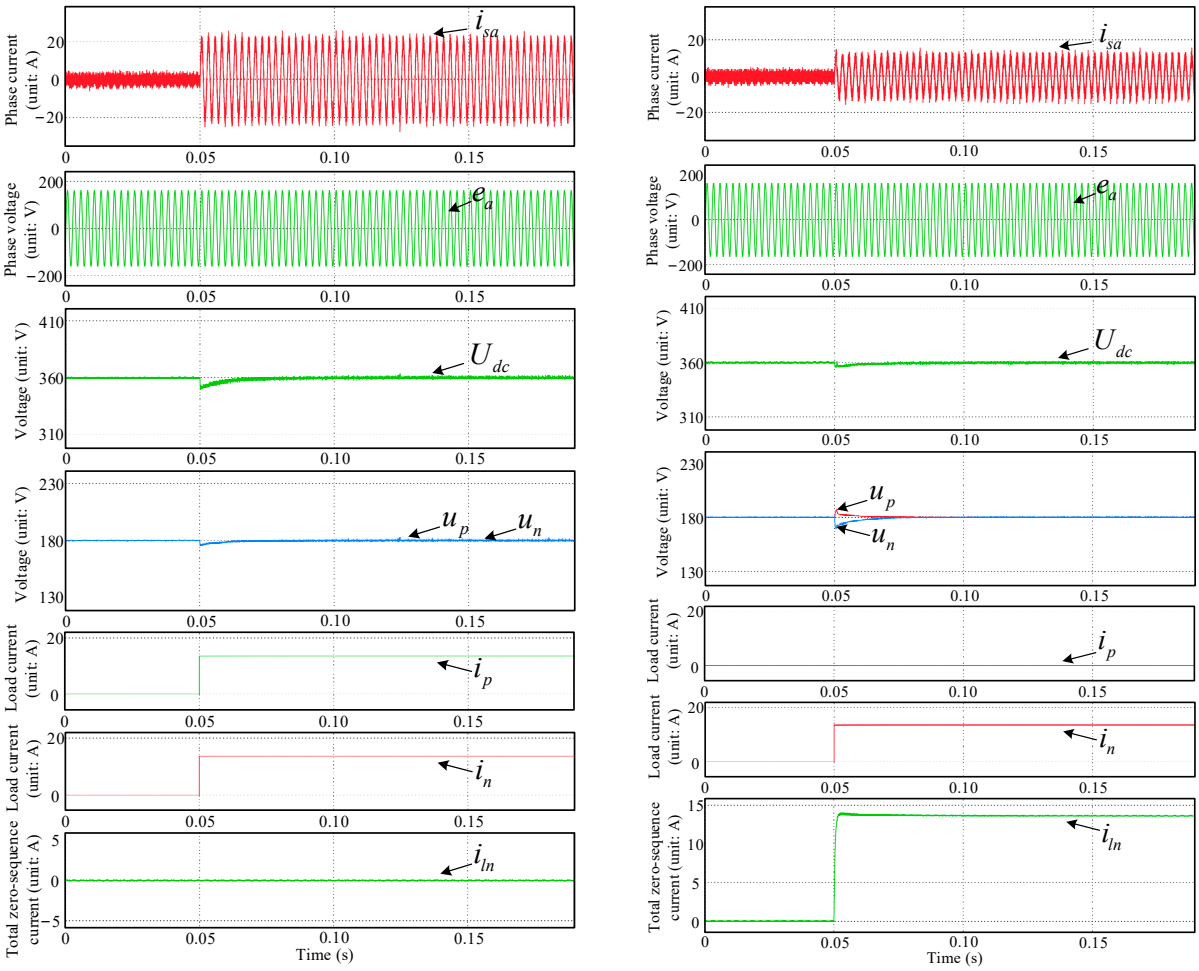

Figure 9. Dynamic simulation results of the proposed VVB-DPC strategy. (**a**) Under balanced load condition. (**b**) Under unbalanced load condition.

6. Experimental Results

6.1. Experimental Prototype and Parameters

In order to verify the feasibility and effectiveness of the proposed VVB-DPC strategy, an experimental prototype of the TCIBAR is established in the laboratory, as shown in Figure 10. The digital signal processor (DSP) TMS320F28335 is selected as the main control chip of the control unit, and the sampling frequency is set as 20 kHz. The rated parameters of the experimental prototype are the same as those listed in Table 6. In the experimental prototype, the positive and negative port capacitances are designed based on the requirement of voltage drop suppression during load step, and the filter inductance is selected to reduce the high-frequency harmonics of the phase current. Meanwhile, the self-inductance and mutual inductance of the TCI are designed to meet the demands of low power loss and fast dynamic response of zero-sequence current [18]. In addition, a

three-phase programmable AC source is used to generate the three-phase source voltages instead of a generator.

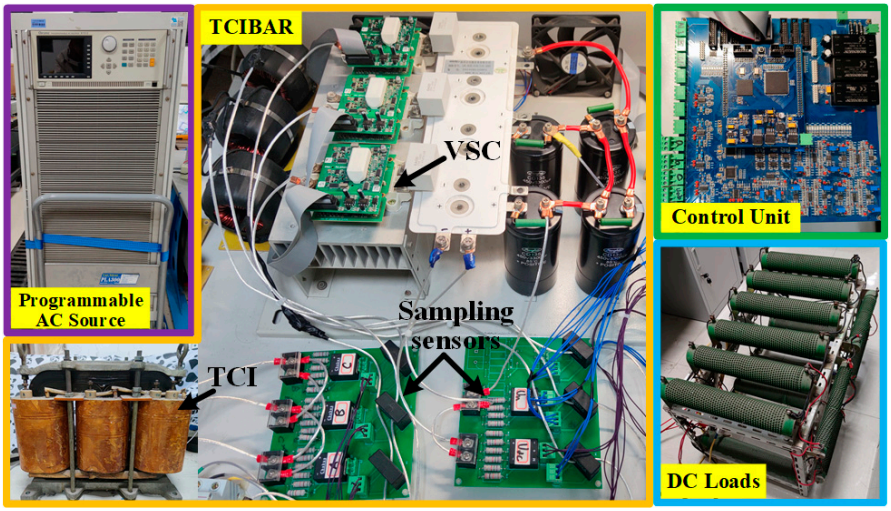

Figure 10. Experimental prototype of TCIBAR.

6.2. Steady-state Experimental Research

In order to test the feasibility of the proposed virtual-vector switching table for VVB-DPC, the comparative experiments of the classic switching table (Table 1) and the proposed virtual-vector switching table (Table 4) were carried out on the prototype under no-load condition, and the experimental results are shown in Figure 11.

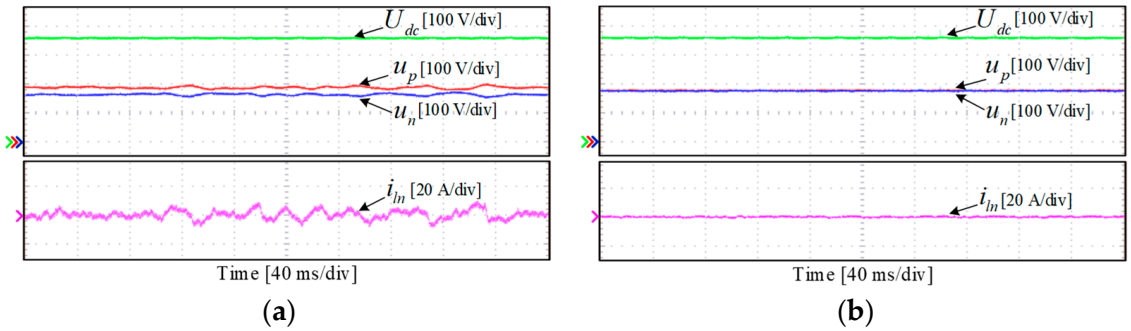

Figure 11. Steady-state experimental results of different switching tables under no-load condition. (**a**) Classic switching table. (**b**) Proposed virtual-vector switching table.

It can be seen from Figure 11a that, if the classic switching table is used for the hysteresis power control of TCIBAR, the DC bus voltage can still be stabilized. However, since the influence of the ZSV components in basic voltage vectors on the TCIBAR is not taken into account, the zero-sequence current i_{l0} in TCI is uncontrolled. Thus, the total zero-sequence current (i_{ln}) injected into the DC-side neutral point fluctuates greatly, which further leads to the fluctuation of the DC-side neutral-point potential and the voltage imbalance between the positive and negative DC ports.

Compared with the experimental results in Figure 11a, the proposed virtual-vector switching table can not only maintain the stability of the DC bus voltage, but it also realizes the effective control of the zero-sequence current in TCI, as shown in Figure 11b. The total zero-sequence current i_{ln} can be maintained at 0 A stably, and the voltage balance between the bipolar DC ports is achieved. Therefore, the experimental results in Figure 11 validate the feasibility and effectiveness of the proposed virtual-vector switching table.

Next, in order to research the steady-state performance of the neutral-point potential control method in the proposed VVB-DPC strategy, the experiments under unbalanced load condition have be performed on the prototype of the TCIBAR. Meanwhile, to create the unbalanced load condition, only the negative port of the TCIBAR carries a 13.3 Ω resistive load, while the positive port is unloaded. The experimental results before and after the adoption of the proposed neutral-point potential control method under unbalanced load condition are shown in Figures 12 and 13, respectively.

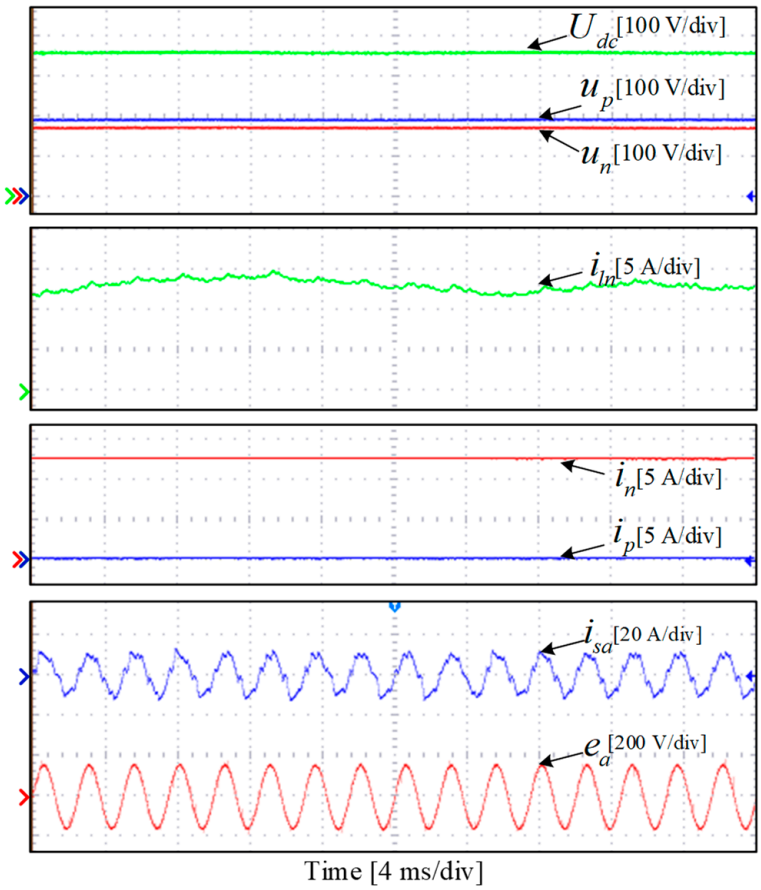

Figure 12. Steady-state experimental results of TCIBAR without the proposed neutral-point potential control method under unbalanced load condition.

As shown in Figure 12, since the ZSV across the TCI cannot be controlled actively, the zero-sequence current in TCI cannot be regulated accurately, and there exists a large fluctuation in the total zero-sequence current i_{ln}. Meanwhile, the DC voltages of the positive and negative ports are not balanced, and the voltage difference is about 20 V.

Based on the proposed neutral-point potential control method, the zero-sequence current in TCI can be controlled effectively and stabilized at about 13.5 A, as shown in Figure 13. Besides, it can be seen that the voltage balance between the bipolar DC ports of the TCIBAR can still be maintained under unbalanced load condition. Therefore, combining the virtual-vector switching table and the neutral-point potential control method, the proposed VVB-DPC strategy can realize the effective control of the TCIBAR and has good steady-state performance even under unbalanced load conditions.

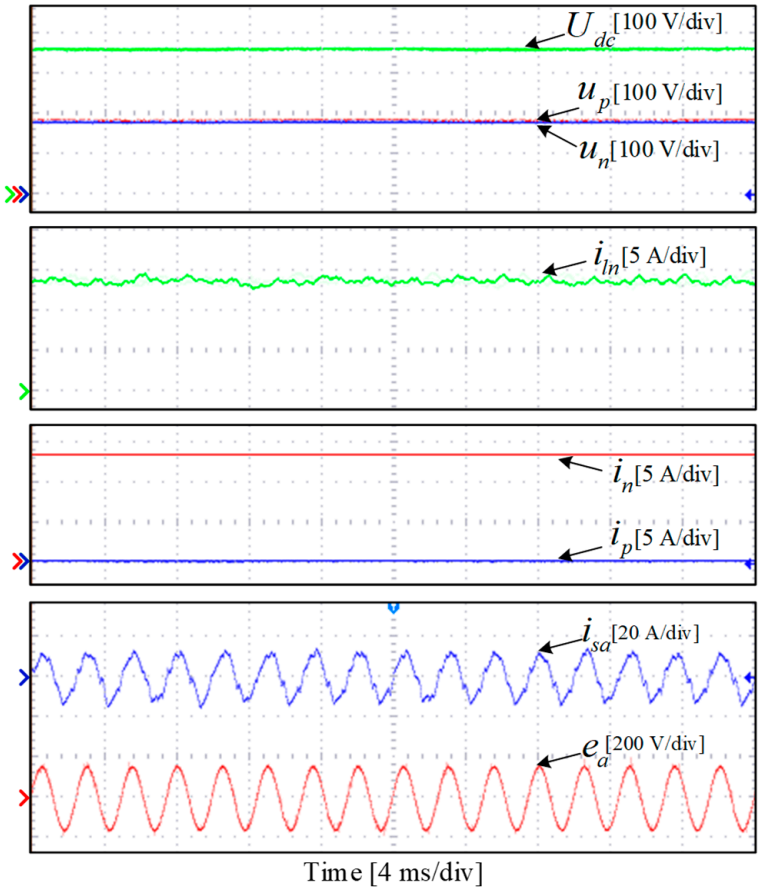

Figure 13. Steady-state experimental results of TCIBAR with the proposed neutral-point potential control method under unbalanced load condition.

6.3. Dynamic Experimental Research

In order to research the dynamic performance of the proposed VVB-DPC strategy, the experiments with step loads have been performed under balanced and unbalanced load conditions. In addition, the balanced load condition is built by connecting 13.3 Ω resistors to both the positive and negative ports of the TCIBAR, while only a 13.3 Ω resistor will be connected to the negative port in the unbalanced load condition.

The experimental results of the balanced step loads are shown in Figure 14. As can be seen, when the balanced step loads are connected to the bipolar DC ports of the TCIBAR, a voltage drop of about 16 V occurs on the DC bus. Owing to the proposed VVB-DPC strategy, the TCIBAR can respond immediately and increase the phase currents in time to realize the fast tracking of the load power. As shown in Figure 14, the DC bus voltage drop caused by the step loads can be compensated within 20 ms, and the DC bus voltage is restored to the rated value. Meanwhile, during the whole dynamic process, the TCIBAR can maintain the voltage balance between the positive and negative ports, and the total zero-sequence current i_{ln} can be controlled at 0 A stably.

Figure 15 shows the dynamic experimental results of the unbalanced step loads. As can be seen from Figure 15, the total DC bus voltage drops by about 10 V when the unbalanced loads are switched on. Moreover, since the loads are severely unbalanced, a potential drift occurs at the DC-side neutral point of the TCIBAR, which further leads to a voltage imbalance between the positive and negative DC ports. Meanwhile, the maximum voltage difference between the DC ports is about 25 V in the dynamic process. With the proposed VVB-DPC strategy, the TCIBAR can make a quick response to the unbalanced load step. On the one hand, the phase currents of the TCIBAR are increased immediately once the voltage drop of DC bus is detected, and the DC bus voltage can be restored to the rated

value within 10 ms. On the other hand, by actively regulating the zero-sequence current in TCI, the neutral-point potential drift can be eliminated, and the DC voltages of the positive and negative ports are rebalanced within 30 ms.

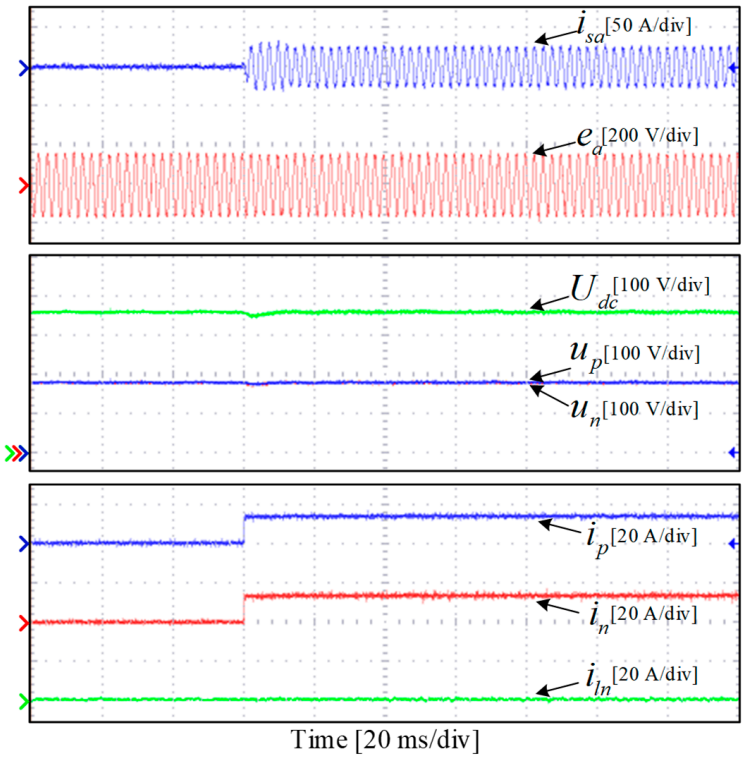

Figure 14. Dynamic experimental results of the proposed VVB-DPC strategy under balanced step load condition.

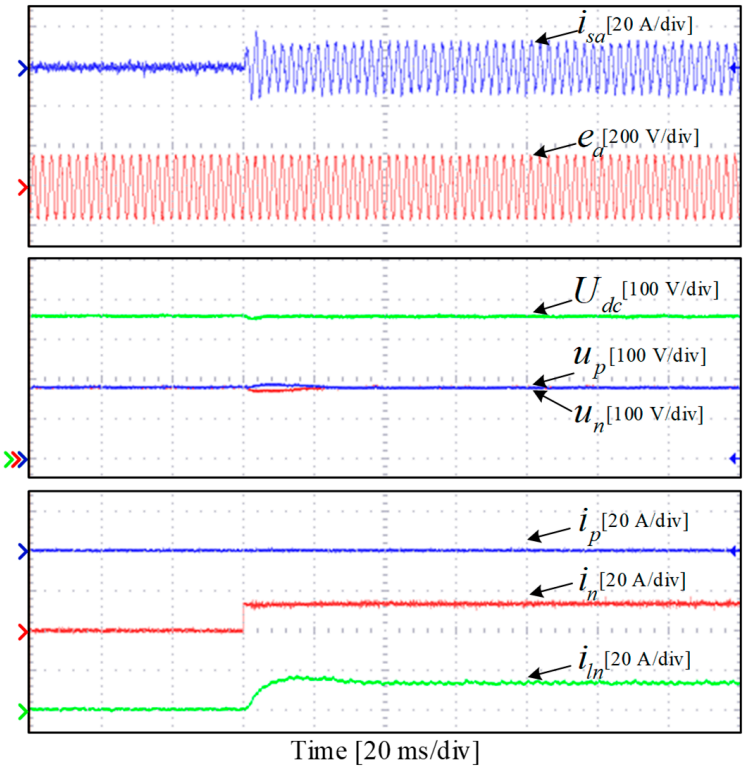

Figure 15. Dynamic experimental results of the proposed VVB-DPC strategy under unbalanced step load condition.

The above load step experimental results show that the proposed VVB-DPC strategy has good dynamic performance on the power control and neutral-point potential control of the TCIBAR, and it can adapt well to both the balanced and unbalanced load conditions. In addition, the experimental results of the proposed VVB-DPC strategy are consistent with the simulation results in Section 5.

7. Conclusions

In this paper, a VVB-DPC strategy is presented for the TCIBAR. Based on the proposed VVB-DPC strategy, the TCIBAR can generate the balanced bipolar DC power supply for MEA under different load conditions. Compared to the classic DPC strategy, the proposed VVB-DPC strategy adopts the derived virtual vectors to establish a new switching table for TCIBAR, and the derived virtual vectors can realize the hysteresis power control of TCIBAR without causing the runaway of the zero-sequence current in TCI. Meanwhile, the proposed VVB-DPC strategy incorporates the neutral-point potential control of the TCIBAR. By inserting an appropriate zero vector with a certain duty ratio in one control cycle, the voltage balance between the bipolar DC ports of the TCIBAR can be maintained even under unbalanced load conditions. The experimental results prove the feasibility and effectiveness of the proposed VVB-DPC strategy in the power control and neutral-point potential control of the TCIBAR. Thus, the proposed VVB-DPC strategy can be considered as a competitive scheme to promote the application of the TCIBAR in the power supply system of future MEAs.

Author Contributions: Conceptualization, methodology, software, validation, formal analysis, investigation, writing—original draft preparation and visualization, Y.Z.; resources, data curation, and supervision, Y.Z. and W.H.; writing—review and editing, Y.Z., W.H. and F.B.; funding acquisition, F.B. All authors have read and agreed to the published version of the manuscript.

Funding: This research was funded by the National Natural Science Foundation of China under Grant 52177050.

Data Availability Statement: Not applicable.

Conflicts of Interest: The authors declare no conflict of interest.

References

1. Wheeler, P.; Bozhko, S. The more electric aircraft: Technology and challenges. *IEEE Electrif. Mag.* **2014**, *2*, 6–12. [CrossRef]
2. Rajashekara, K. Power conversion technologies for automotive and aircraft systems. *IEEE Electrif. Mag.* **2014**, *2*, 50–60. [CrossRef]
3. Emadi, K.; Ehsani, M. Aircraft power systems: Technology, state of the art, and future trends. *IEEE Aero. Electron. Sys. Mag.* **2000**, *15*, 28–32. [CrossRef]
4. Roboam, X. New trends and challenges of electrical networks embedded in more electrical aircraft. In Proceedings of the IEEE International Symposium on Industrial Electronics, Gdansk, Poland, 27–30 June 2011.
5. Li, W.; Yang, Y.; Zhang, X. Digital generator control unit design for a variable frequency synchronous generator in MEA. *Energies* **2018**, *11*, 96. [CrossRef]
6. Lei, T.; Min, Z.; Gao, Q.; Song, L.; Zhang, X.; Zhang, X. The architecture optimization and energy management technology of aircraft power systems: A review and future trends. *Energies* **2022**, *15*, 4109. [CrossRef]
7. Chen, J.W.; Wang, C.; Chen, J. Investigation on the selection of electric power system architecture for future more electric aircraft. *IEEE Trans. Transp. Electrif.* **2018**, *4*, 563–576. [CrossRef]
8. Sarlioglu, B.; Morris, C.T. More electric aircraft: Review, challenges, and opportunities for commercial transport aircraft. *IEEE Trans. Transp. Electrif.* **2015**, *1*, 54–64. [CrossRef]
9. Jia, Y.; Rajashekara, K. Induction machine for more electric aircraft: Enabling new electrical power system architectures. *IEEE Electrif. Mag.* **2017**, *5*, 25–37. [CrossRef]
10. Karanayil, B.; Ciobotaru, M.; Agelidis, V.G. Power flow management of isolated multiport converter for more electric aircraft. *IEEE Trans. Power Electron.* **2017**, *32*, 5850–5861. [CrossRef]
11. Ojeda-Rodriguez, A.; Gonzalez-Vizuete, P.; Bernal-Mendez, J.; Martin-Prats, M.A. A survey on bidirectional DC/DC power converter topologies for the future hybrid and all electric aircrafts. *Energies* **2020**, *13*, 4883. [CrossRef]
12. Brombach, J.; Lucken, A.; Nya, B.; Johannsen, M.; Schulz, D. Comparison of different electrical HVDC architectures for aircraft application. In Proceedings of the Electrical Systems for Aircraft, Railway and Ship Propulsion, Bologna, Italy, 16–18 October 2012.

13. Roboam, X.; Sareni, B.; Andrade, A.D. More electricity in the air: Toward optimized electrical networks embedded in more-electrical aircraft. *IEEE Ind. Electron. Mag.* **2012**, *6*, 6–17. [CrossRef]
14. Madonna, V.; Giangrande, P.; Galea, M. Electrical power generation in aircraft: Review, challenges, and opportunities. *IEEE Trans. Transp. Electrif.* **2018**, *4*, 646–659. [CrossRef]
15. Nuutinen, P.; Pinomaa, A.; Peltoniemi, P.; Kaipia, T.; Karppanen, J.; Silventoinen, P. Common-mode and RF EMI in a low-voltage DC distribution network with a PWM grid-tie rectifying converter. *IEEE Trans. Smart Grid* **2017**, *8*, 400–408. [CrossRef]
16. Wang, F.; Lei, Z.; Xu, X.; Shu, X. Topology deduction and analysis of voltage balancers for DC microgrid. *IEEE J. Emerg. Sel. Top. Power Electron.* **2017**, *5*, 672–680. [CrossRef]
17. Perera, C.; Salmon, J.; Kish, G.J. Multiport converter with independent control of ac and dc power flows for bipolar dc distribution. *IEEE Trans. Power Electron.* **2021**, *36*, 3473–3485. [CrossRef]
18. Li, Y.; Junyent-Ferre, A.; Rodriguez-Bernuz, J.M. A three-phase active rectifier topology for bipolar dc distribution. *IEEE Trans. Power Electron.* **2018**, *33*, 1063–1074. [CrossRef]
19. Zhao, Y.; Huang, W.; Bu, F. DC voltage balancing strategy of a bipolar-output active rectifier for more electric aircraft based on zero vector redistribution. *IEEE Access* **2021**, *9*, 139657–139667. [CrossRef]
20. Zhang, Y.; Qu, C. Direct power control of a pulse width modulation rectifier using space vector modulation under unbalanced grid voltages. *IEEE Trans. Power Electron.* **2015**, *30*, 5892–5901. [CrossRef]
21. Malinowski, M.; Kazmierkowski, M.P.; Hansen, S.; Blaabjerg, F.; Marques, G.D. Virtual-flux-based direct power control of three-phase PWM rectifiers. *IEEE Trans. Ind. Appl.* **2001**, *37*, 1019–1027. [CrossRef]
22. Zhang, Y.; Jiao, J.; Liu, J.; Gao, J. Direct power control of PWM rectifier with feedforward compensation of DC-bus voltage ripple under unbalanced grid conditions. *IEEE Trans. Ind. Appl.* **2019**, *55*, 2890–2901. [CrossRef]
23. Yan, S.; Yang, Y.; Hui, S.Y.; Blaabjerg, F. A review on direct power control of pulsewidth modulation converters. *IEEE Trans. Power Electron.* **2021**, *36*, 11984–12007. [CrossRef]
24. Escobar, G.; Stankovic, A.M.; Carrasco, J.M.; Galvan, E.; Ortega, R. Analysis and design of direct power control (DPC) for a three phase synchronous rectifier via output regulation subspaces. *IEEE Trans. Power Electron.* **2003**, *18*, 823–830. [CrossRef]
25. Noguchi, T.; Tomiki, H.; Kondo, S.; Takahashi, I. Direct power control of PWM converter without power-source voltage sensors. *IEEE Trans. Ind. Appl.* **1998**, *34*, 473–479. [CrossRef]
26. Ge, J.; Zhao, Z.; Yuan, L.; Lu, T.; He, F. Direct power control based on natural switching surface for three-phase PWM rectifiers. *IEEE Trans. Power Electron.* **2015**, *30*, 2918–2922. [CrossRef]
27. Sato, A.; Noguchi, T. Voltage-source PWM rectifier–inverter based on direct power control and its operation characteristics. *IEEE Trans. Power Electron.* **2011**, *26*, 1559–1567. [CrossRef]
28. Alonso-Martinez, J.; Carrasco, J.E.; Arnaltes, S. Table-based direct power control: A critical review for microgrid applications. *IEEE Trans. Power Electron.* **2010**, *25*, 2949–2961. [CrossRef]
29. Zhang, Y.; Qu, C.; Gao, J. Performance improvement of direct power control of PWM rectifier under unbalanced network. *IEEE Trans. Power Electron.* **2017**, *32*, 2319–2328. [CrossRef]
30. Baktash, A.; Vahedi, A.; Masoum, M.A.S. Improved switching table for direct power control of three-phase PWM rectifier. In Proceedings of the Australasian Universities Power Engineering Conference, Perth, WA, Australia, 9–12 December 2007.
31. Bouafia, A.; Gaubert, J.P.; Krim, F. Analysis and design of new switching table for direct power control of three-phase PWM rectifier. In Proceedings of the 13th International Power Electronics and Motion Control Conference, Poznan, Poland, 1–3 September 2008.
32. Zhang, Y.; Qu, C. Table-based direct power control for three-phase AC/DC converters under unbalanced grid voltages. *IEEE Trans. Power Electron.* **2015**, *30*, 7090–7099. [CrossRef]
33. Kong, X.; Yuan, Y.; Li, P.; Wang, Y.; Lin, J. The design and analysis of the PI regulator of three-phase voltage source PWM rectifier. In Proceedings of the 2015 IEEE Region 10 Conference, Macao, China, 1–4 November 2015.
34. Wei, K.; Wang, S. Modeling and simulation of three-phase voltage source PWM rectifier. In Proceedings of the International Conference on Advanced Computer Theory and Engineering, Phuket, Thailand, 20–22 December 2008.